In vivo albumin labeling and lymphatic imaging

Yu Wang[a,b], Lixin Lang[b], Peng Huang[b], Zhe Wang[b], Orit Jacobson[b], Dale O. Kiesewetter[b], Iqbal U. Ali[b], Gaojun Teng[a,1], Gang Niu[b,1], and Xiaoyuan Chen[b,1]

[a]Jiangsu Key Laboratory of Molecular Imaging and Functional Imaging, Department of Radiology, Zhongda Hospital, Medical School of Southeast University, Nanjing 210009, China; and [b]Laboratory of Molecular Imaging and Nanomedicine, National Institute of Biomedical Imaging and Bioengineering, National Institutes of Health, Bethesda, MD 20892

Edited* by Michael E. Phelps, University of California, Los Angeles, CA, and approved November 25, 2014 (received for review August 5, 2014)

The ability to accurately and easily locate sentinel lymph nodes (LNs) with noninvasive imaging methods would assist in tumor staging and patient management. For this purpose, we developed a lymphatic imaging agent by mixing fluorine-18 aluminum fluoride-labeled NOTA (1,4,7-triazacyclononane-*N,N′,N″*-triacetic acid)-conjugated truncated Evans blue (^{18}F-AlF-NEB) and Evans blue (EB) dye. After local injection, both ^{18}F-AlF-NEB and EB form complexes with endogenous albumin in the interstitial fluid and allow for visualizing the lymphatic system. Positron emission tomography (PET) and/or optical imaging of LNs was performed in three different animal models including a hind limb inflammation model, an orthotropic breast cancer model, and a metastatic breast cancer model. In all three models, the LNs can be distinguished clearly by the apparent blue color and strong fluorescence signal from EB as well as a high-intensity PET signal from ^{18}F-AlF-NEB. The lymphatic vessels between the LNs can also be optically visualized. The easy preparation, excellent PET and optical imaging quality, and biosafety suggest that this combination of ^{18}F-AlF-NEB and EB has great potential for clinical application to map sentinel LNs and provide intraoperative guidance.

PET | lymph node | optical imaging | albumin | Evans blue

The lymphatic system plays a key role in maintaining tissue interstitial pressure by collecting protein-rich fluid that is extracted from capillaries (1). The lymphatic system is also a critical component of the immune system. Many types of malignant tumors such as breast cancer, melanoma, and prostate cancer are prone to metastasize in regional lymph nodes (LNs), possibly through tumor-associated lymphatic channels (2, 3). The status of these sentinel LNs (SLNs) not only provides a marker for tumor staging but also serves as an indicator of prognosis (4). Consequently, detection and mapping of SLNs is a key step in therapeutic decision-making (5).

One common method used in the clinic is a two-step procedure that consists of local administration of radionuclide-labeled colloids, mostly with technetium-99m, several hours before the injection of a vital dye such as Patent blue (isosulfan blue). SLNs can be visualized either by gamma scintigraphy or single photon emission computed tomography. The SLNs during surgery can be located with a hand-held gamma ray counter and visual contrast of the blue dye (6–8). However, this method requires separate administration of two agents because of different rates of local migration of the colloidal particles and blue dye molecules (9). Due to the relatively low sensitivity and poor spatial resolution of scintigraphy and single photon emission computed tomography, it is highly desirable to develop new imaging probes for other imaging modalities. The objective is to improve the detection of SLNs for either noninvasive visualization or intrasurgical guidance (10–14).

Recently, imaging-guided surgery, especially with fluorescent probes, has been intensively studied due to its low cost, simplicity, and adaptability (15). The limited tissue penetration of light is less critical because of the open field of view during surgery (16). For example, NIR fluorescence dyes, such as indocyanine green, have been investigated for sentinel node navigation during surgery either alone or in combination with nanoformulations (13, 14). Owing to the nanometer-scale size, stability, and strong fluorescence, various nanoparticles and nanoformulations have been applied for SLN imaging and showed promising results in preclinical models (10–12). However, most of these probes are composed of heavy metals, making their clinical translation difficult due to the acute and chronic toxicity (17). In addition, scattering and tissue attenuation cause poor results for presurgical evaluation of SLNs using optical imaging.

Evans blue (EB) is an azo dye, which can bind quantitatively to serum albumin, and has been used for nearly a century to determine blood plasma volume and extravascular protein leakage in patients (18). Indeed, EB also showed promise in LN mapping in both clinical practice and preclinical studies (19, 20). In this respect, ^{99m}Tc–EB appears to be better than ^{99m}Tc–antimony trisulfide colloid/Patent Blue V dual injection in discriminating the SLN (21, 22). Recently, we synthesized a NOTA (1,4,7-triazacyclononane-N,N′,N″-triacetic acid)-conjugated truncated EB (NEB). ^{18}F-labeling was achieved through the formation of the ^{18}F-aluminum fluoride (^{18}F-AlF) complex. The whole labeling process takes only around 20–30 min without the need of HPLC purification (23). After i.v. injection, ^{18}F-AlF-NEB complexed with serum albumin very quickly, and thus, most of the radioactivity was restrained to the blood circulation. ^{18}F-AlF-NEB has been successfully applied to evaluate cardiac function in a myocardial infarction model and vascular permeability in inflammatory and tumor models (23).

Although primarily an intravascular protein, albumin cyclically leaves the circulation through the endothelial barrier at the level of the capillaries. The albumin concentration in the interstitial fluid is around 20–30% of that in the plasma, and back transport of proteins from the interstitial fluid to the plasma is accomplished mainly by the lymphatic system (24). After local administration, NEB forms a complex with albumin in the interstitial

Significance

The imaging agent we developed in this study can be used for visualization and detection of sentinel lymph nodes (SLNs). After local injection, the imaging probe quickly formed a complex with albumin within the interstitial fluid. Thus, the radioactive signal reflects the behavior of endogenous albumin, avoiding the usage of colloids, nanoparticles, or polymers. The SLNs can be visualized by PET scans before surgery and then removed under the guidance of fluorescence signal and blue color deposit during surgery. The excellent imaging quality, easy preparation, multimodality, and biosafety guarantee the clinical translation to map SLNs and provide intraoperative guidance.

Author contributions: Y.W., G.T., G.N., and X.C. designed research; Y.W., L.L., P.H., Z.W., O.J., and D.O.K. performed research; L.L. contributed new reagents/analytic tools; Y.W., Z.W., G.N., and X.C. analyzed data; and Y.W., D.O.K., I.U.A., G.N., and X.C. wrote the paper.

The authors declare no conflict of interest.

*This Direct Submission article had a prearranged editor.

[1]To whom correspondence may be addressed. Email: shawn.chen@nih.gov, gjteng@vip.sina.com, or niug@mail.nih.gov.

This article contains supporting information online at www.pnas.org/lookup/suppl/doi:10.1073/pnas.1414821112/-/DCSupplemental.

www.pnas.org/cgi/doi/10.1073/pnas.1414821112

fluid and travels through the lymphatic system. In this study, we mixed ^{18}F-AlF-NEB with EB (^{18}F-AlF-NEB/EB) to perform multimodal imaging of LNs in different animal models via a single administration. Although PET provides a presurgical evaluation of SLNs, fluorescence signal and visible blue color afford guidance for surgery.

Results

PET Imaging of Inflamed LNs. ^{18}F-AlF-NEB PET imaging was performed on day 5 after turpentine injection. As shown in Fig. 1*A*, popliteal LNs on both sides were clearly seen on PET images with a high signal to background ratio at all of the time points examined. Due to the inflammatory stimulation, the left popliteal LNs had an obviously higher tracer uptake than the contralateral normal LNs. The left sciatic LNs also showed slightly higher signal intensity. Corresponding T_2-weighted MRIs confirmed swelling of the popliteal LNs (Fig. 1*B*) but not the sciatic LNs. Overlay of PET images with X-ray confirmed the anatomic location of the popliteal LNs (Fig. 1*C*). Quantification of the PET images showed that uptake of ^{18}F-AlF-NEB in the left popliteal LN was 0.195 ± 0.039%ID (percentage injected dose), which was significantly higher than that in the right popliteal LN (0.09 ± 0.035%ID, $P < 0.05$) at 0.5 h postinjection. The signal intensity in the left popliteal LN dropped to 0.116 ± 0.052%ID at the 3-h time point (Fig. 1*D*). As shown in Fig. 1*E*, although the left sciatic LN had somewhat higher tracer uptake than the right sciatic LN, no significant difference was found ($P > 0.05$).

PET Imaging of Tumor-Draining LNs. Thirty days after tumor inoculation, female nude mice bearing orthotropic MDA-MB-435 breast cancer tumors were scanned following intratumoral injection of ^{18}F-AlF-NEB. As shown in Fig. 2 *A*–*C*, besides the tracer injection site, a satellite spot with high signal intensity was identified on PET images from three orientations (coronal, sagittal, and transaxial) of the same mouse. Using a reference map of the lymphatic system of a rodent mammary fat pad (25), the hot spot was identified as the accessory axillary LN. To confirm this, one mouse was killed after PET imaging, and the right accessory axillary LN was removed (Fig. 2*D*). An ex vivo PET image showed that a tumor-draining axillary LN had an apparent uptake of ^{18}F-AlF-NEB (Fig. 2*E*). Furthermore, another hot spot was observed in the neck area, which, according to the anatomy of murine LNs, might be an LN belonging to the cervical LN group (Fig. 2*F*). We also performed PET imaging of mice at day 60 after tumor inoculation; both the axillary LN and the cervical LN could be detected by ^{18}F-AlF-NEB PET (Fig. S1 *A* and *B*). However, no tumor metastasis was observed with H&E staining of axillary LNs (Fig. S1*C*).

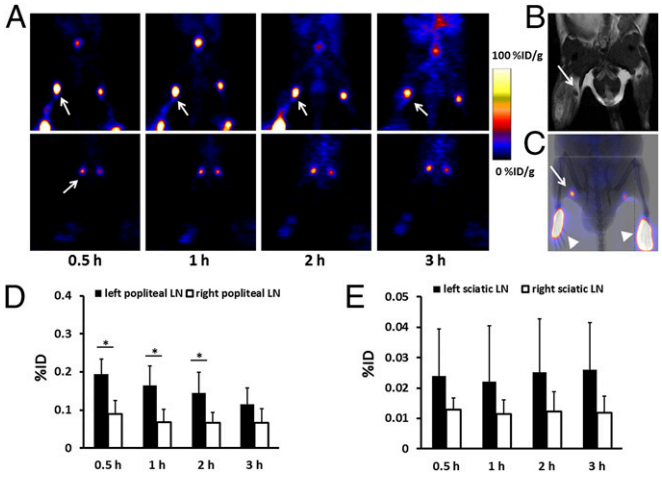

Fig. 1. (*A*) Representative reconstructed coronal PET images of inflamed popliteal (*Upper*) and sciatic (*Lower*) LNs in the turpentine oil-induced hind limb inflammation model. LNs were pointed out by white arrows. (*B*) T_2-weighted MRI shows an enlarged inflamed popliteal LN, as indicated by a white arrow. (*C*) Overlay of PET with a 2D X-ray image. The LN is indicated by a white arrow and the injection sites by arrowheads. (*D*) Quantitative analysis based on the PET images. There is significantly higher total tracer uptake in inflamed popliteal LNs than that of contralateral normal LNs at 0.5, 1, 2, and 3 h after tracer injection (*$P < 0.05$). (*E*) Quantitative analysis of tracer uptake in sciatic LNs. No statistical significance was found between LNs in the left and right side.

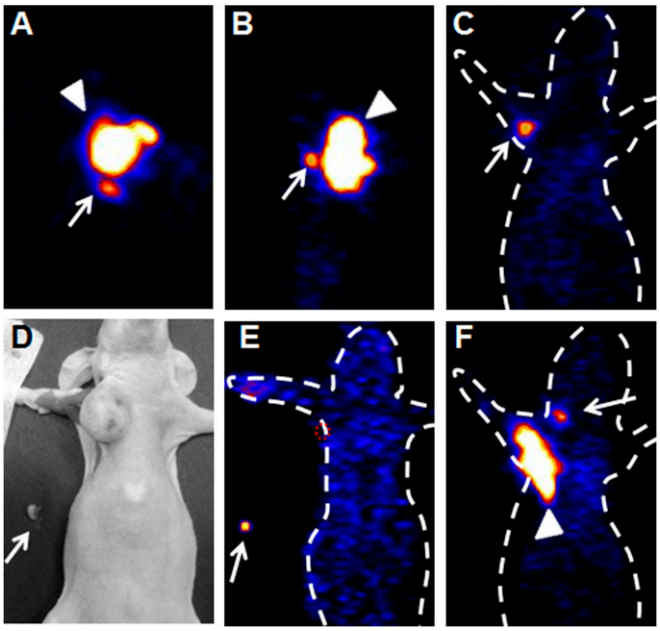

Fig. 2. (*A*–*C*) Representative ^{18}F-AlF-NEB PET images of an axillary LN in the orthotropic breast cancer model (*A*, transaxial; *B*, sagittal; *C*, coronal images). PET scans were performed at 30 min after tracer injection. Arrows indicate tumor-draining axillary LNs, and arrowheads indicate primary tumors. A white dotted line was added to indicate animal contour. (*D* and *E*) Photograph (*D*) and ex vivo PET image (*E*) confirmed tracer uptake of an ipsilateral axillary LN after intratumoral injection of ^{18}F-AlF-NEB. (*F*) Coronal image shows a cervical LN. Arrows indicate tumor-draining axillary LNs, and arrowheads indicate primary tumors.

PET Imaging of Metastatic LNs. We also applied ^{18}F-AlF-NEB PET to image tumor metastatic LNs. Four weeks after inoculation of Fluc$^+$ 4T1 cells via hock injection, an obvious bioluminescence signal could be seen at the popliteal fossa by bioluminescence imaging (BLI) (Fig. 3*A*). A T_2-weighted MRI also showed enlarged tumor-side popliteal LNs (Fig. 3*B*). Immunofluorescence staining with antiluciferase antibody confirmed the existence of tumor metastasis in the left popliteal LN (Fig. 3*C*). The average long-axis diameter of the left LN measured by MRI was also significantly larger than that of the right one (Fig. S2).

^{18}F-AlF-NEB PET was performed 1 d after the MRI. Both popliteal LNs could be visualized in four out of six mice. As seen in Fig. 3*D*, there was a dramatically higher tracer uptake in tumor-draining popliteal LNs compared with the contralateral LNs at all of the time points measured. Additionally, the signal intensity of the left LNs remained high after 1 h and then decreased slowly over a 3-h period. The contralateral LNs showed a similar trend but with much lower signal intensity. Autoradiography at 3 h after the tracer injection displayed heterogeneity of tracer distribution inside the LN. The decreased radioactivity area observed on the LN slice may be due to local tumor metastasis (Fig. 3*E*). Quantitative results demonstrated that the total tracer uptake of tumor

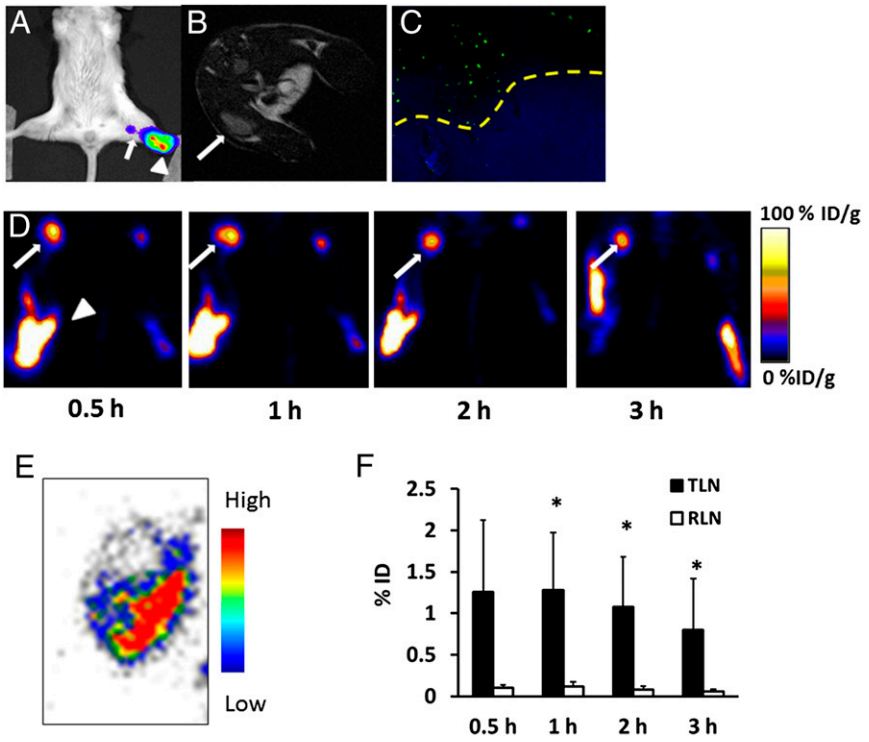

Fig. 3. (*A*) Representative BLI imaging of a metastatic popliteal LN (white arrow) located near the primary tumor (white arrowhead). (*B*) Axial T_2-weighted MRI shows an enlarged metastatic popliteal LN, as indicated by a white arrow. (*C*) Immunofluorescence staining confirmed the existence of metastasis in the popliteal LN. Yellow dashed line differentiates metastasis (*Upper*) from normal lymphatic tissue (*Lower*). (*D*) Representative coronal PET images of metastatic popliteal LNs (white arrows) at different time points after local injection of ^{18}F-AlF-NEB. White arrowheads indicate the injection site. (*E*) Autoradiography confirmed the metastasis (cold area) in the popliteal LN. (*F*) Quantitative analysis of the total tracer uptake in tumor-draining LN (TLN) and right side normal LN (RLN). The value was corrected by the weights of LNs (*$P < 0.05$).

metastatic LNs dropped slightly with time from 0.5 to 3 h. The values were significantly higher than those of LNs from the right side (Fig. 3*F*). In two of the six mice, no apparent tracer uptake in the tumor-side popliteal LNs was detected. However, both the sciatic and inguinal LNs from the tumor side could be clearly seen on PET images and had much higher signal intensity than the LNs on the contralateral side (Fig. 4 *A* and *B*). To confirm the quantitative PET results, an ex vivo biodistribution study was carried out, and the results are presented in Fig. S3. Thirty minutes after the tracer injection, the majority of radioactivity remained at the injection sites in both paws. Consistent with PET, direct tissue sampling showed significantly higher tracer accumulation in the left popliteal LNs than that in the contralateral LNs ($P < 0.05$).

Tumor metastasis in the draining LNs was confirmed by H&E staining. As shown in Fig. 4*C*, healthy LNs consisted of mainly immune cells with relatively large nuclei and a small amount of cytoplasm. Conversely, part of the tumor-draining LNs, especially in the subscapular sinus area, was occupied by cells with irregular nuclei, which were tumor-metastatic foci (Fig. 4*D*). Foci of micrometastasis were also found inside some of the tumor-draining LNs (Fig. S4).

Multimodal Imaging of LNs. Because NEB showed similar albumin binding compared with EB dye (23), we performed LN visual imaging after coinjection of ^{18}F-AlF-NEB and EB. Ninety minutes after local injection, both popliteal LN sites could be distinguished clearly by the apparent blue color, indicating the local accumulation of the dye molecules. The left sciatic LNs could also be seen but with much lower uptake of dye (Fig. 5 *A* and *B*). There was a significant difference in weight between the popliteal LNs on the tumor side and the contralateral side but not between the sciatic LNs (popliteal LNs, 3.582 ± 0.762 vs. 1.995 ± 0.759 mg, $P < 0.05$; sciatic LNs, 1.558 ± 0.731 vs. 1.403 ± 0.632 mg, $P > 0.05$) (Fig. 5*C*). The total amount of EB dye in

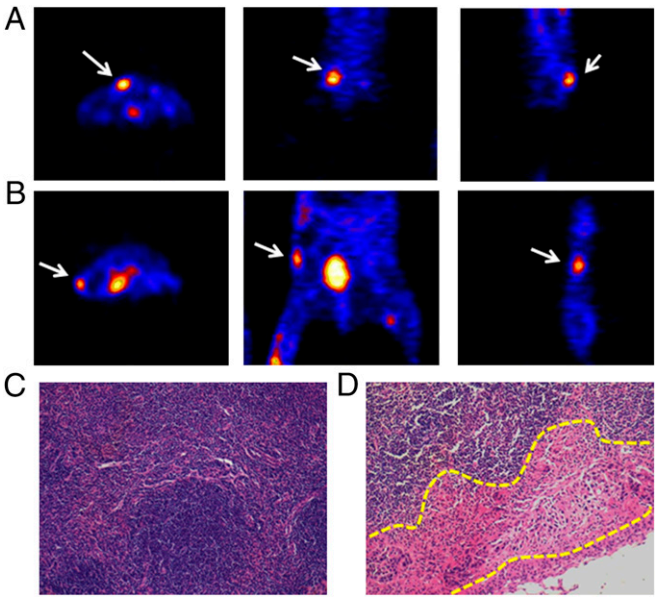

Fig. 4. (*A* and *B*) Representative PET images show high tracer uptake in sciatic LN (*A*) or inguinal LN (*B*). Three sections of the same LN were presented (from left to right, transaxial, coronal, and sagittal). (*C* and *D*) H&E stain of a healthy popliteal LN (*C*) and a metastatic LN (*D*). Yellow dashed line delineates metastasis foci at the subscapular sinus area.

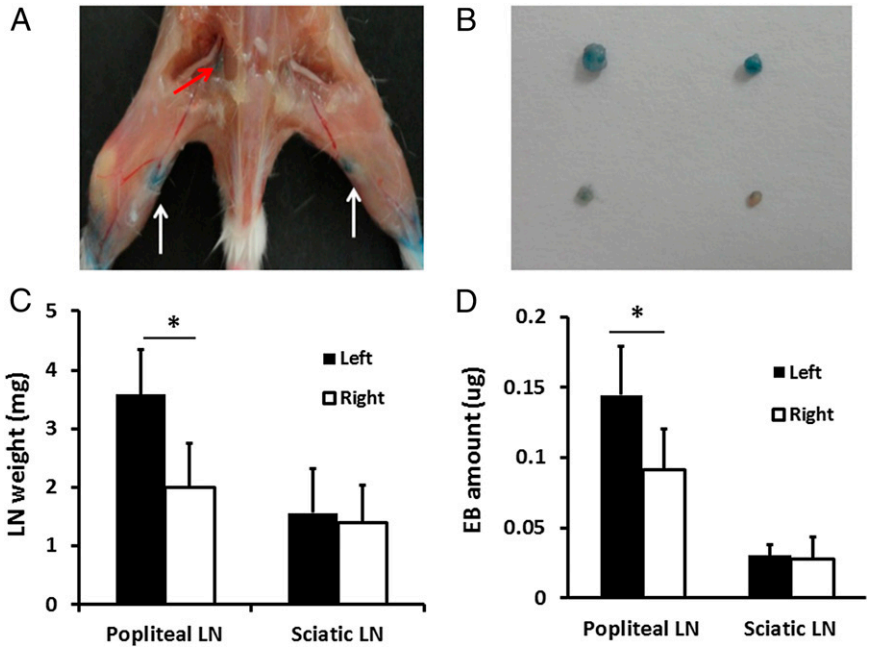

Fig. 5. (*A*) LN mapping with EB dye in a turpentine oil-induced hind limb inflammation model. White arrows indicate popliteal LNs with blue color, and red arrows show the light blue left sciatic LN. (*B*) Photograph of excised LNs. The upper two are popliteal LNs, and the lower two are sciatic LNs. LNs on the left side are harvested from the inflamed hind limb, whereas those on the right side are from a normal limb. (*C*) Quantitative analysis of LN size based on its weight (*$P < 0.05$). (*D*) UV measurement showed the difference of EB amount in different LNs (*$P < 0.05$).

each group of LNs was measured, and the results are shown in Fig. 5*D*. Left popliteal LNs contained 0.144 ± 0.034 μg of EB dye on average, which was significantly higher than that of the right ones (0.091 ± 0.029 μg, $P < 0.05$). However, there was no difference in the amount of EB between two sciatic LNs (0.030 ± 0.008 μg vs. 0.028 ± 0.015 μg, $P > 0.05$). These ex vivo results were consistent with in vivo PET data.

After forming a complex with serum albumin, both NEB and EB became fluorescent (23, 26). Because we mixed only a trace amount of NEB with EB, the majority of the fluorescence came from EB. EB showed a strong absorbance peak at 620 nm with or without albumin. However, with only albumin, EB had a fluorescence emission peak at 680 nm (Fig. S5). With optical imaging, the migration of the injected EB/NEB in lymphatics could be clearly observed after local injection. The fluorescence signal first reached the popliteal LN and then migrated to the sciatic LN (Fig. 6*A*). Ninety minutes after tracer injection, both LNs were clearly visualized by fluorescence optical imaging. Under bright light, apparent blue dye accumulation could also be seen by the naked eye (Fig. 6 *B* and *C*). We also performed PET and optical imaging with the same animal after injection of ^{18}F-AlF-NEB/EB. An overlay of the two images provided high positional correlation of the LNs (Fig. 6 *D* and *E*).

Discussion

We have developed an innovative lymphatic imaging agent by mixing EB with the PET tracer ^{18}F-AlF-NEB. EB has been extensively used as a visible dye. In fact, the quantum yield of EB itself is rather low. However, like some other dye molecules, when EB forms a complex with albumin, the fluorescence emission of the complex increases dramatically (Fig. S2). It is widely accepted that albumin binding sterically and electronically stabilizes the fluorophore's ground state electronic distribution and increases the quantum yield (27). In fact, the fluorescence signal is more sensitive than the visible color. We took advantage of this phenomenon and performed fluorescence imaging after local injection of ^{18}F-AlF-NEB/EB, which quickly forms a complex with albumin within the interstitial fluid. The radioactive signal reflects the behavior of endogenous albumin, avoiding the use of colloids, nanoparticles, and polymers. Thus, mixing ^{18}F-AlF-NEB with the EB dye allows PET, visual, and fluorescence trimodality imaging. Local LNs and the lymphatic vessels between LNs can be clearly visualized by the blue color of the dye as well as optical imaging. Furthermore, the SLNs can be detected by PET scans.

As a proof of concept, we first applied this imaging probe to a turpentine oil-induced hind limb inflammation model. With inflammatory stimulation, local LNs undergo a series of changes to clear debris and provide a site for activated immune cells. This process is often coupled with an increase in size and enhanced lymphatic drainage (28). Turpentine oil induced the tissue inflammatory responses peak at day 4 (29). Therefore, we first performed ^{18}F-AlF-NEB PET imaging in the hind limb inflammation model on day 5 after turpentine oil injection. The popliteal and sciatic LNs on both sides can be clearly visualized from 0.5 to 3 h after tracer injection, with inflamed LNs accumulating a higher amount of tracer (Fig. 1). The imaging results corroborate with the size and flow changes during local inflammatory responses. We next explored the feasibility of imaging tumor-draining LNs in an orthotropic breast tumor model. After intratumoral injection, SLNs were successfully detected by ^{18}F-AlF-NEB PET with excellent image quality (Fig. 2).

The detection of SLNs is important in clinical cancer classification and treatment (30). Currently, presurgical diagnosis of SLNs is often based on the morphological changes observed by MR or CT scans. However, it is very challenging for MRI or CT to visualize SLNs when they are very small or have signal intensities comparable with surrounding healthy soft tissues (31). Based on our imaging results acquired in three different animal models, we believe that coinjection of ^{18}F-AlF-NEB and EB can be applied clinically for SLN detection. After local administration, PET imaging can be performed first to identify the distribution and location of SLNs around the tumor. Then the surgeon can rely on visible blue color and fluorescence imaging

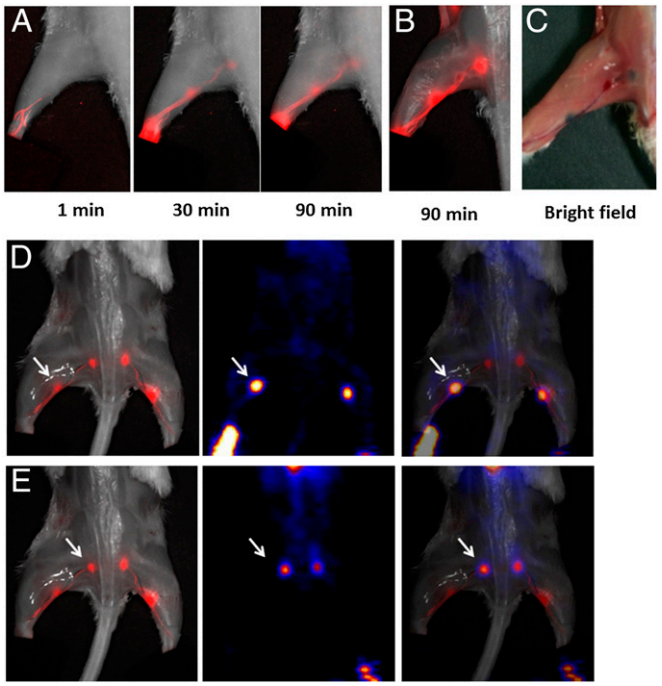

Fig. 6. (*A*) Longitudinal fluorescence imaging of the lymphatic system after hock injection of ^{18}F-AlF-NEB/EB. LNs and lymphatic vessels can be clearly seen with the migration of the tracer along with time. (*B*) Ex vivo optical imaging of LNs without skin. (*C*) Photograph of the same mice to show the blue color within the LNs. (*D*) Coregistration of optical image (*Left*) and PET image (*Middle*) to present the popliteal LNs, indicated by a white arrow. (*E*) Coregistration of optical image (*Left*) and PET image (*Middle*) to present the sciatic LNs, indicated by a white arrow. The mice were euthanized at 90 min after hock injection of ^{18}F-AlF-NEB/EB and the skin was removed.

during surgery for SLN biopsy and removal. A hand-held detector can also be used for SLN detection.

One limitation of ^{18}F-AlF-NEB/EB is that this strategy may not be used directly to visualize tumor metastasis, although increased tracer accumulation can be observed in some tumor-draining LNs (32). Indeed, several tumor-draining LNs were not visible on PET images described in this study. Histology showed that these LNs were fully occupied by tumor cells with no lymphatic function and that the afferent lymphatic vessels toward the LNs were blocked by metastatic tumors. It is of note that visualization of tumor-draining LNs using lymphatic mapping agents is time- and stage-dependent (10, 32). At the very early stage, when no tumor metastasis exists, the growth of the primary tumor induces a local inflammatory reaction and the tumor-draining LNs undergo hyperplasia, with stimulation of cytokines secreted by the primary tumor. Over time, tumor cells disseminate to LNs and form micrometastases. Hyperplasia and lymphocyte infiltration lead to high uptake of ^{18}F-AlF-NEB/EB in the LNs. However, at the very late stage, when the normal lymph tissue was fully occupied by tumor tissue or when metastatic tumor tissue blocks the lymphatic flow, little to no tracer uptake will be observed. In this case, morphological CT and MRI or ^{18}F-FDG PET (33) may improve the detection of metastatic LNs.

To the best of our knowledge, this is the first time that a small molecular PET tracer has been used to image LNs. The trimodality imaging provides an excellent, noninvasive presurgical visualization of SLNs as well as intrasurgical guidance. The multimodal PET imaging tracer that we developed has great potential for clinical application due to its biosafety, excellent quality of imaging, easy preparation, and cost-effectiveness.

Conclusion

Coinjection of ^{18}F-AlF-NEB and EB provides an easy method of in vivo labeling of endogenous albumin in the interstitial fluid, thereby enabling PET, optical fluorescence, and visual trimodality imaging for highly sensitive detection of LNs and lymphatic vessels. The excellent imaging quality, easy preparation, multimodal applicability, and biosafety of this approach warrant its clinical application to map SLNs and provide intraoperative guidance.

Materials and Methods

Synthesis of ^{18}F-AlF-NEB. [^{18}F]F$^-$ radionuclide was obtained from the National Institutes of Health (NIH) Clinical Center's cyclotron facility by proton irradiation of ^{18}O-enriched water. The chemical synthesis and radiolabeling of NEB has been reported in our previous study (23). The radiochemical yield for ^{18}F-AlF-NEB was around 60%, with a total synthesis and work-up time of 20–30 min.

Animal Models. All animal studies were conducted in accordance with the principles and procedures outlined in the Guide for the Care and Use of Laboratory Animals (34) and were approved by the Institutional Animal Care and Use Committee of the Clinical Center, NIH.

BALB/c mice (n = 6) were used to develop the hind limb inflammation model, with 10 μL of turpentine oil intramuscularly injected into the left leg. MRI and PET were performed on day 5 after injection according to the time course of inflammatory responses (29, 35).

MDA-MB-435 cells were maintained at 37 °C in a humidified atmosphere containing 5% CO_2 in Leibovitz's L-15 medium (Thermo Scientific) with 10% (vol/vol) FBS (Gibco, CA), 100 IU/mL of penicillin, and 100 μg/mL of streptomycin (Invitrogen). For establishment of the orthotropic breast cancer model, 5×10^6 MDA-MB-435 cells in 100 μL of PBS were injected into the right mammary pad of female nude mice (n = 4). PET scans were performed at 30 and 60 d after tumor inoculation.

4T1 murine breast cancer cells with stable transfection of the firefly luciferase reporter gene were cultured in Dulbecco's Modified Eagle's Medium with 10% (vol/vol) FBS (Gibco), 100 IU/mL of penicillin, and 100 μg/mL of streptomycin (Invitrogen). For the LN metastasis model, 5×10^5 fLuc$^+$ 4T1 cells in 30 μL of PBS were injected into the left hock area of Balb/C mice (n = 6). BLI was performed weekly to monitor the tumor growth and metastases. MRI was performed at 4 wk after tumor inoculation, followed by ^{18}F-AlF-NEB PET imaging 1 d later.

MRI. MRI was performed on a high magnetic field micro-MR scanner (7.0 T, Bruker, Pharmascan) with small animal-specific body coil. Mice were anesthetized by isoflurane (3% for induction and 2–3% for maintenance) and kept warm by a circulating water pad. T_2-weighted images were obtained by a multislice multiecho (MSME) sequence with the following parameters: repetition time (TR), 2,500 ms; effective echo time (TE), 45 ms; number of excitations (NEX), 1; matrix size, 256 × 256; field of view (FOV), 3 × 3 cm; slice thickness, 1 mm. A magnetic resonance-compatible small animal respiratory gating device was used to reduce the artifacts caused by respiration. The long axis diameter of each LN was measured on the T_2-weighted images and used for size quantification.

Bioluminescence Imaging. 4T1 tumor-bearing mice were subjected to BLI weekly using a Lumina II imaging system (Caliper Life Sciences) to observe the progression of metastasis. Mice were anesthetized by 2% isofluorane, followed by i.p. injection of 150 mg/kg D-luciferin diluted in 100 μL of normal saline. BLI was performed 10 min after injection, and the acquisition time was 5 min.

PET. All PET scans were performed with an Inveon PET scanner (Siemens Preclinical Solutions). During acquisition, the mice were anesthetized by 2% (vol/vol) isoflurane. For the hind limb inflammation study, 0.37 MBq (10 μCi) of ^{18}F-AlF-NEB in 10 μL of saline was mixed with 2.5 mg/mL of sterile EB solution, then injected into the footpad of each side of the inflamed mice (n = 6). Static PET scans were acquired at 0.5, 1, 2, and 3 h after tracer injection. The acquisition time was 5 min at 0.5 h and 10 min at the other time points. Both the left (inflamed) and right (normal) LNs were harvested after the last acquisition for quantifying EB concentration.

For the orthotropic breast cancer model, tumor-bearing mice were subjected to PET imaging on day 30 (n = 4) and day 60 (n = 1) after tumor inoculation. A single dose of 0.37 MBq (10 μCi) of ^{18}F-AlF-NEB in 20 μL of sterile saline was injected intratumorally. After injection, the syringes were held for

1–2 min to prevent backflow of the tracer through the injection site. A 10-min static PET acquisition was performed at 30 min after tracer injection.

For the 4T1 tumor metastasis model, 0.37 MBq (10 μCi) of ^{18}F-AlF-NEB, either in 10 μL of saline premixed with 10 μL EB (2.5 mg/mL) solution ($n = 3$) or in 20 μL of saline only ($n = 3$), was injected into both the left and right footpads of each mouse. Static PET scans were acquired at 0.5, 1, 2, and 3 h after tracer injection. The acquisition time was 5 min at 0.5 h and 10 min at the other time points. After imaging, all mice were killed and the LNs from both sides were harvested for autoradiography and histologic staining. For mice injected with the mixture of ^{18}F-AlF-NEB and EB, optical imaging was performed.

All images were reconstructed using a 3D ordered subset expectation maximum algorithm. Images were analyzed with Inveon Research Workplace (Siemens Preclinical Solution). The 3D ellipsoidal regions of interest were manually defined on targeted LNs of each mouse. The accumulation of radioactivity was then calculated and expressed as %ID/g. This value was then multiplied by LN weight and expressed as %ID.

Quantification of EB. Both LNs in the inflammatory side and the contralateral side were weighed before being put into 20 μL of formamide for EB extraction. After centrifugation, the supernatant of each tube was carefully removed, and the light absorbance at 620 nm was measured with a NanoDrop 2000 Spectrophotometer (Thermo Fisher Scientific Inc.). The concentration of EB was calculated using a standard absorption curve for known concentrations of EB mixed with albumin.

Autoradiography. Metastatic LNs were embedded in an optimum cutting temperature compound (Sakura Finetek) and sectioned to slices with a thickness of 10 μm for autoradiography. The tissue slices were exposed to a high-efficiency storage phosphor screen overnight at –80 °C, and the screen was developed in a Cyclone Plus storage phosphor system (PerkinElmer). The autoradiographs were analyzed with Optiquant 5.0 (Perkin-Elmer).

Optical Imaging. In vivo optical imaging was performed using a Maestro II small animal optical imaging system (Cambridge Research & Instrumentation) with a Green filter set (excitation, 523 nm; emission, 635 nm long pass). We injected 0.37 MBq (10 μCi) of ^{18}F-AlF-NEB, in 10 μL of saline premixed with 10 μL of EB (2.5 mg/mL) solution, into both the left and right hocks of each mouse. Imaging was performed at 1, 5, 10, 15, 30, 45, 60, and 90 min after the injection of the probe ($n = 3$ per group). During the injection and image acquisition process, the mice were anesthetized with 2% (vol/vol) isoflurane in oxygen delivered at a flow rate of 1.0 L/min. At 90 min after injection, the mice were killed, and ex vivo PET and optical imaging was performed.

Immunohistology. Tissue slices of metastatic LNs were fixed by cold acetone, and then blocked with PBS containing 1% BSA for 30 min. The slices were incubated with rabbit antiluciferase primary antibody (1:100, Abcam) for 1 h at room temperature, followed by incubation with Dylight 488-conjugated donkey anti-rabbit secondary antibody (1:200; Jackson ImmunoResearch Laboratories) for 40 min at room temperature. After each step, slices were washed gently with PBS containing 0.05% tween 20 (PBST) for 5 min three times. All slices were mounted with mounting medium containing 4′, 6-diamidino- 2-phenylindole and then observed by an epifluorescence microscope (X81; Olympus).

For H&E staining, all slices were fixed with buffered zinc formalin fixatives (Z-fix, Anatech LTD) and then embedded in paraffin. The sections were stained with H&E as previously described (36).

Statistical Analysis. All data were expressed as mean ± SD. Statistical analysis was performed with Excel software (version 2010, Microsoft Inc.). Student t test was used for two-group comparisons at different time points. $P < 0.05$ was considered statistically significant.

ACKNOWLEDGMENTS. This work was supported by the Intramural Research Program of the National Institute of Biomedical Imaging and Bioengineering, NIH.

1. Swartz MA (2001) The physiology of the lymphatic system. *Adv Drug Deliv Rev* 50(1-2):3–20.
2. Picker LJ, Butcher EC (1992) Physiological and molecular mechanisms of lymphocyte homing. *Annu Rev Immunol* 10:561–591.
3. Karaman S, Detmar M (2014) Mechanisms of lymphatic metastasis. *J Clin Invest* 124(3): 922–928.
4. Tammela T, Alitalo K (2010) Lymphangiogenesis: Molecular mechanisms and future promise. *Cell* 140(4):460–476.
5. Veronesi U, et al. (1997) Sentinel-node biopsy to avoid axillary dissection in breast cancer with clinically negative lymph-nodes. *Lancet* 349(9069):1864–1867.
6. Wilhelm AJ, Mijnhout GS, Franssen EJ (1999) Radiopharmaceuticals in sentinel lymph-node detection—An overview. *Eur J Nucl Med* 26(4, Suppl):S36–S42.
7. Mariani G, et al. (2001) Radioguided sentinel lymph node biopsy in breast cancer surgery. *J Nucl Med* 42(8):1198–1215.
8. Mariani G, et al. (2002) Radioguided sentinel lymph node biopsy in malignant cutaneous melanoma. *J Nucl Med* 43(6):811–827.
9. Tsopelas C, Sutton R (2002) Why certain dyes are useful for localizing the sentinel lymph node. *J Nucl Med* 43(10):1377–1382.
10. Huang X, et al. (2012) Long-term multimodal imaging of tumor draining sentinel lymph nodes using mesoporous silica-based nanoprobes. *Biomaterials* 33(17): 4370–4378.
11. Kim S, et al. (2004) Near-infrared fluorescent type II quantum dots for sentinel lymph node mapping. *Nat Biotechnol* 22(1):93–97.
12. Verbeek FP, et al. (2014) Near-infrared fluorescence sentinel lymph node mapping in breast cancer: A multicenter experience. *Breast Cancer Res Treat* 143(2):333–342.
13. Hirano A, et al. (2012) A comparison of indocyanine green fluorescence imaging plus blue dye and blue dye alone for sentinel node navigation surgery in breast cancer patients. *Ann Surg Oncol* 19(13):4112–4116.
14. Koo J, et al. (2012) In vivo non-ionizing photoacoustic mapping of sentinel lymph nodes and bladders with ICG-enhanced carbon nanotubes. *Phys Med Biol* 57(23): 7853–7862.
15. Chi C, et al. (2014) Intraoperative imaging-guided cancer surgery: From current fluorescence molecular imaging methods to future multi-modality imaging technology. *Theranostics* 4(11):1072–1084.
16. Nguyen QT, Tsien RY (2013) Fluorescence-guided surgery with live molecular navigation—A new cutting edge. *Nat Rev Cancer* 13(9):653–662.
17. Sengupta J, Ghosh S, Datta P, Gomes A, Gomes A (2014) Physiologically important metal nanoparticles and their toxicity. *J Nanosci Nanotechnol* 14(1):990–1006.
18. Cody HS, 3rd (1999) Sentinel lymph node mapping in breast cancer. *Breast Cancer* 6(1):13–22.
19. Kern KA (1999) Sentinel lymph node mapping in breast cancer using subareolar injection of blue dye. *J Am Coll Surg* 189(6):539–545.
20. Harrell MI, Iritani BM, Ruddell A (2008) Lymph node mapping in the mouse. *J Immunol Methods* 332(1-2):170–174.
21. Sutton R, Tsopelas C, Kollias J, Chatterton BE, Coventry BJ (2002) Sentinel node biopsy and lymphoscintigraphy with a technetium 99m labeled blue dye in a rabbit model. *Surgery* 131(1):44–49.
22. Tsopelas C, et al. (2006) ^{99m}Tc-Evans blue dye for mapping contiguous lymph node sequences and discriminating the sentinel lymph node in an ovine model. *Ann Surg Oncol* 13(5):692–700.
23. Niu G, et al. (2014) In vivo labeling of serum albumin for PET. *J Nucl Med* 55(7): 1150–1156.
24. Ellmerer M, et al. (2000) Measurement of interstitial albumin in human skeletal muscle and adipose tissue by open-flow microperfusion. *Am J Physiol Endocrinol Metab* 278(2):E352–E356.
25. Van den Broeck W, Derore A, Simoens P (2006) Anatomy and nomenclature of murine lymph nodes: Descriptive study and nomenclatory standardization in BALB/cAnNCrl mice. *J Immunol Methods* 312(1-2):12–19.
26. Niu G, Li Z, Xie J, Le QT, Chen X (2009) PET of EGFR antibody distribution in head and neck squamous cell carcinoma models. *J Nucl Med* 50(7):1116–1123.
27. Wolfe LS, et al. (2010) Protein-induced photophysical changes to the amyloid indicator dye thioflavin T. *Proc Natl Acad Sci USA* 107(39):16863–16868.
28. Swartz MA, Hubbell JA, Reddy ST (2008) Lymphatic drainage function and its immunological implications: From dendritic cell homing to vaccine design. *Semin Immunol* 20(2):147–156.
29. Yamada S, Kubota K, Kubota R, Ido T, Tamahashi N (1995) High accumulation of fluorine-18-fluorodeoxyglucose in turpentine-induced inflammatory tissue. *J Nucl Med* 36(7):1301–1306.
30. Tokin CA, et al. (2012) The efficacy of Tilmanocept in sentinel lymph mode mapping and identification in breast cancer patients: A comparative review and meta-analysis of the mTc-labeled nanocolloid human serum albumin standard of care. *Clin Exp Metastasis* 29(7):681–686.
31. Tiguert R, et al. (1999) Lymph node size does not correlate with the presence of prostate cancer metastasis. *Urology* 53(2):367–371.
32. Zhang F, Zhu L, Huang X, Niu G, Chen X (2013) Differentiation of reactive and tumor metastatic lymph nodes with diffusion-weighted and SPIO-enhanced MRI. *Mol Imaging Biol* 15(1):40–47.
33. Pieterman RM, et al. (2000) Preoperative staging of non-small-cell lung cancer with positron-emission tomography. *N Engl J Med* 343(4):254–261.
34. Anonymous (2010) *Guide for the Care and Use of Laboratory Animals* (National Academy Press, Washington, DC).
35. Wu C, et al. (2014) Longitudinal PET imaging of muscular inflammation using 18F-DPA-714 and 18F-Alfatide II and differentiation with tumors. *Theranostics* 4(5): 546–555.
36. Ruscher K, et al. (2013) Inhibition of CXCL12 signaling attenuates the postischemic immune response and improves functional recovery after stroke. *J Cereb Blood Flow Metab* 33(8):1225–1234.